ISA Transactions 52 (2013) 105–114

Contents lists available at SciVerse ScienceDirect

ISA Transactions

journal homepage: www.elsevier.com/locate/isatrans

High-precision control of LSRM based X–Y table for industrial applications

J.F. Pan [a], Norbert C. Cheung [b,*], Yu Zou [a]

[a] Department of Automation Science, College of Mechatronics and Control Engineering, Shenzhen University, 3688, Nanhai Road, Shenzhen, Guangdong Province, PR China
[b] Hong Kong Polytechnic University, Department of Electrical Engineering, Hunghom, Kowloon, Hong Kong

ARTICLE INFO

Article history:
Received 16 December 2011
Received in revised form
31 July 2012
Accepted 13 August 2012
Available online 12 September 2012

Keywords:
Direct-drive
Linear switched reluctance motor
Adaptive control
Parameter identification

ABSTRACT

The design of an X–Y table applying direct-drive linear switched reluctance motor (LSRM) principle is proposed in this paper. The proposed X–Y table has the characteristics of low cost, simple and stable mechanical structure. After the design procedure is introduced, an adaptive position control method based on online parameter identification and pole-placement regulation scheme is developed for the X–Y table. Experimental results prove the feasibility and its priority over a traditional PID controller with better dynamic response, static performance and robustness to disturbances. It is expected that the novel two-dimensional direct-drive system find its applications in high-precision manufacture area.

1. Introduction

Modern industrial automatic systems usually require high-speed or high-precision linear motions. This is often realized by rotary motors coupled with mechanical translators, such as gears or belts for rotary to linear motion transformation. Such mechanical transmissions not only reduce linear performance, but also introduce backlash, frictional and inertial loads to the system [1]. With the fast development of power electronics and motion control algorithms, direct-drive machines have aroused researchers' attention. In a direct-drive system, electrical energy is directly converted into mechanical output, eliminating any mechanical translators. With the direct coupling method, the mechanical structure of the actuator can be greatly simplified and the whole system will be easy to assemble, reduced in cost and increased in performance.

For linear direct-drive machines, linear permanent magnet motors (LPMMs), linear induction motors (LIMs) and linear switched reluctance motors (LSRMs) are commonly available. Similar to a rotary induction machine, the LIM has a robust mechanical structure and a smooth force output can be obtained under proper control algorithms. However, a high air gap flux density is difficult to be developed and the large end effects impose a severe control burden to the system [2]. Among all types of linear machines, a LPMM has relatively high efficiency and larger speed regulation range; therefore, it is a viable candidate to meet the increasing demands for high accuracy in industrial applications. Since LPMMs rely on permanent magnets for magnetic force production, inevitably, system cost is high and the temperature range of operation is limited, due to the characteristics of permanent magnets. Furthermore, LPMMs are more easily affected by load disturbances, force ripples and parameter variations, etc., which significantly deteriorate system performance [3].

Switched reluctance motors (SRMs) have the advantages of simple structure, high robustness, and absence of permanent magnets. Though the control of the SRM is complex, due to the highly nonlinear characteristics inherent in the magnetic path, SRMs have been successfully applied in many high-precision speed regulation fields [4–6]. Compared to LPMMs, LSRMs have a relatively low power density, nevertheless, the simple and robust structure and the low system implementation cost make them a feasible alternative for LPMMs in low-speed, high-precision applications in industry. In this paper, a design method of LSRM-based two-dimensional (2D) X–Y machine is introduced.

Industrial manufacturing environment is filled with many kinds of disturbances such as coupled interferences, unmeasured frictions, external load disturbances and unmodeled dynamics, etc. Therefore a proper measure should be taken for correct detection and compensation of disturbances in real-time. It is very difficult for a traditional proportion–integral–derivative (PID) controller to cope with disturbances and variations since its design is mainly based on the static model of the system [7]. Therefore a control algorithm of disturbance detection and real-time compensation should be introduced to overcome this deficiency. Based on previous study and research, the authors successfully implement an adaptive approach with online

* Corresponding author.
E-mail addresses: pan_jian_fei@163.com (J.F. Pan), norbert.cheung@polyu.edu.hk (N.C. Cheung).

0019-0578/$ - see front matter © 2012 ISA. Published by Elsevier Ltd. All rights reserved.
http://dx.doi.org/10.1016/j.isatra.2012.08.001

parameter identification on the LSRM-based X–Y machine to correct disturbances and mechanical imperfections, increasing robustness for system operation.

2. Design and construction

The LSRMs applied for the X–Y machine has a "passive-stator–active-mover" structure and this arrangement has the following advantages [8],

1. Simple manufacture of the stator base without complicated coil arrays
2. Flexible traveling range and stator dimensions
3. Easy manufacture of mover slots with mounted coil windings

Since the X–Y machine is designed for low-speed, high-precision applications, to meet with the maximum output force requirement, regardless of end effect, normal and propulsion force in the linear region for each phase can be derived from the following equations as [9],

$$f_z(s,i) = -\frac{\mu_0 l N^2 i^2 (d-s)}{2z^2} \tag{1}$$

$$f_x(s,i) = \frac{\pi \times i^2 \times L_\Delta}{p} \times \sin\left(\frac{2\pi s}{p}\right) \tag{2}$$

where s is travel distance, l is stack length, N is number of turns, i is phase current and $2L_\Delta$ is change of phase inductance from aligned to un-aligned positions. Other parameters are specified in Fig. 1. In general, L_Δ is a function of motor geometry (d,p,l,z). The phase inductance can be represented by the Fourier series. If the first order approximation is considered, the self-inductance is equal to [10],

$$L(x) = L_{ls} + L_0 + L_\Delta \cos\left(\frac{2\pi x}{p}\right) \tag{3}$$

$$L_0 = N^2 \mu_0 l N_s C_0 \tag{4}$$

$$L_\Delta = N^2 \mu_0 l N_s C_1 \tag{5}$$

where L_{ls} is phase leakage inductance and N_s is the number of teeth on a primary side pole. The Fourier coefficients C_0 and C_1 for the normalized permeance of one teeth can be found in a standard table [11] for pole-pitch versus air gap length.

In case of both LSRMs, N_s is chosen as 2 and air gap length z is chosen to be 0.2 and 0.3 mm for the X and Y direction, respectively, for practical and accurate mechanical manufacture and alignment. Since Y axis carries X axis and bears more weight and load, stack length are selected as twice of that from the X direction. The mechanical dimensions of the proposed machine are summarized in Table 1 and the prototype has been manufactured as shown in Fig. 2 with two sets of LSRMs stacked on top of each other. The stator bases and the movers are manufactured

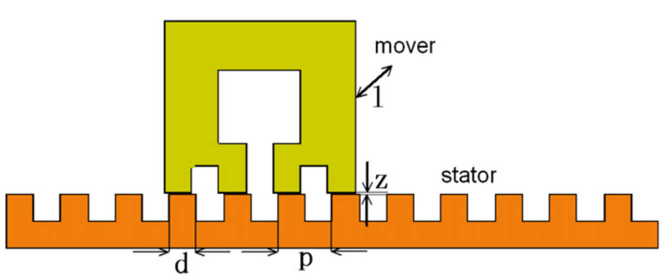

Fig. 1. Definition of motor parameters.

Table 1
Specifications of the prototype.

Traveling distance (X/Y) (mm)	120/170
Air gap (X/Y)—z (mm)	0.2/0.3
Pole-pitch—p (mm)	12
Tooth width—d (mm)	6
Mass of X moving platform—m_x (kg)	1.5
Mass of Y moving platform (not including X platform) —m_y (kg)	2.8
Number of turns per phase—N	160
Stack length—l (mm)	24/48
Encoder resolution (μm)	0.5

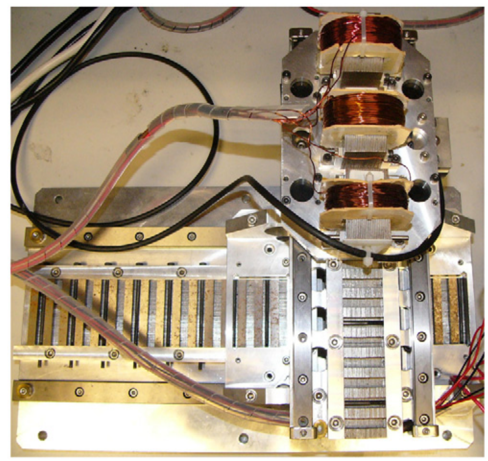

Fig. 2. Prototype of the machine.

with aluminum alloy to reduce total weight. Silicon–steel plates are stacked between the stator and mover slots to facilitate magnetic paths. A pair of linear motion guides ensures smooth sliding motion and supports the moving platform for each axis of motion. Linear optical encoders are mounted on each LSRM to observe motion profile and provide position feedback. The moving platform for each axis of motion is composed of three excitation coils that is consistent with the structure of a typical "6/4" rotary SR motor. Each coil can be driven independently from a magnetically decoupled structure [12]. The coils are separated with 120° electrical degrees to provide phase a, b and c accordingly. From the overall machine construction, since no permanent magnets, ball-screw or mechanical couplings are involved, the manufacturing cost is greatly reduced compared with the rotary motors plus mechanical translators solution or LPMM-based X–Y machines.

3. Theoretical descriptions

3.1. Dynamic model

The mechanical equations that govern the entire motion system can be described in state-space form as follows,

$$\frac{ds_{x(y)}}{dt} = v_{x(y)} \tag{6}$$

$$\frac{dv_{x(y)}}{dt} = (f_{x(y)} - B_{x(y)} v_{x(y)} - f_{lx(y)})/M_{x(y)} \tag{7}$$

where s, v, B, M, f and f_l stand for position, velocity, friction coefficient, mass, total and load force, respectively. Symbol $x(y)$ stands for X axis or Y axis of motion. Eqs. (6) and (7) can be further expressed as

$$M_{x(y)} \times \frac{d^2 s_{x(y)}}{dt^2} + B_{x(y)} \times \frac{ds_{x(y)}}{dt} + f_{lx(y)} = f_{x(y)} \tag{8}$$

For high-precision position control applications, it can be concluded that total force impressed on the moving platform of the X or Y table should be properly regulated. Therefore, the motion control system can be regarded as a single-input–single-output (SISO) system with total force command $f_{x(y)}$ as input and position $s_{x(y)}$ as system output for each axis.

From the electrical side, the kth phase ($k=a,b,c$) can be represented in voltage equation as

$$U_{kx(y)} = R_{kx(y)} \times i_{kx(y)} + \frac{d\lambda_{kx(y)}(s_{x(y)}, i_{kx(y)})}{dt} \tag{9}$$

where $U_{kx(y)}$, $R_{kx(y)}$, and $i_{kx(y)}$ is terminal voltage, coil resistance and current. Rearranging voltage balance equation and neglecting mutual and leakage flux-linkage,

$$\frac{di}{dt} = \frac{U_{kx(y)} - R_{kx(y)} i_{kx(y)} - (\partial\lambda_{kx(y)}/\partial s_{x(y)}) \times (ds_{x(y)}/dt)}{(\partial\lambda_{kx(y)}/\partial i)} \tag{10}$$

As described in article [12], mutual flux-linkage can be neglected from the finite element analysis results. Since the machine is designed for position control applications, typically the control system for each axis of motion can be characterized as a dual-loop control system with current as the inner control loop and position as the outer one [8].

Since real-time operation environment is full of noise and disturbances, the second-order system depicted in Eq. (8) can be further represented in discrete-time form as [13],

$$A(z^{-1}) \times s_{x(y)} = B(z^{-1}) \times f_{x(y)} + e_{x(y)} \tag{11}$$

where $A(z^{-1})$ and $B(z^{-1})$ are polynomials to be determined and $e_{x(y)}$ stands for all unknown disturbances from X and Y axis. Polynomial $A(z^{-1})$ and $B(z^{-1})$ correspond to the typical discrete-time polynomial form as

$$\begin{cases} A(z^{-1}) = 1 + a_1 \times z^{-1} + a_2 \times z^{-2} \\ B(z^{-1}) = b_0 + b_1 \times z^{-1} \end{cases} \tag{12}$$

Therefore, the purpose of online system identification is to correctly estimate a_1, a_2, b_0 and b_1 that contain all dynamic information for each axis.

3.2. Online system identification

Eq. (11) can be considered as a typical least square form below though disturbances may enter at any place into the control system as any form. For nth estimation,

$$s_{x(y)}(t) = \varphi^T(t-1)\theta + e(t) \tag{13}$$

where

$$\begin{cases} \theta = (a_1 a_2 b_0 b_1)^T \\ \varphi^T(t-1) = (-s_{x(y)}(t-1) \cdots -s_{x(y)}(t-n) f_{x(y)}(t) \cdots f_{x(y)}(t-n)) \end{cases} \tag{14}$$

The parameters described in the above equation can be estimated by the recursive least square method as [13],

$$\begin{cases} \hat{\theta}(t) = \hat{\theta}(t-1) + G(t)e(t) \\ G(t) = P(t-1)\varphi(t-1)\left(\rho + \varphi^T(t)P(t-1)\varphi(t)\right)^{-1} \\ P(t) = \left(I - K(t)\varphi^T(t)\right)P(t-1)/\rho \end{cases} \tag{15}$$

Stochastic errors can be represented as

$$e(t) = s_{x(y)}(t) - \varphi^T(t)\hat{\theta}(t-1) \tag{16}$$

where G is the gain and P is the covariance matrix. ρ is the forgetting factor that reflects the relationship between converging rate and tracking ability and it falls into 0 and 1 [13]. A larger forgetting factor represents a more trust on the previous data and low identification sensitivity. For the X–Y machine, ρ is chosen as 0.99 for a fast identification speed and moderate converging ripples for both axis of motion. For initial states, $P(0)$ can be chosen as $r \times I_{4\times4}$ with r as a constant value of 20 and $I_{4\times4}$ is a four-dimension unit matrix. If the relative error from the present and last step is comparatively small, it can be regarded that the present estimated value is correct. Then the criterion to terminate the program for the recursive calculation can be set as

$$\left| \frac{\hat{\theta}(t+1) - \hat{\theta}(t)}{\hat{\theta}(t)} \right| < \zeta \tag{17}$$

where ζ is a small positive number.

3.3. Adaptive controller design based on pole-placement

The adaptive controller design is based on the results of the online parameter identification, which can represent system dynamics of the machine in real-time. Based on the pole-placement algorithm, the structure of the proposed adaptive controller can be depicted as shown in Fig. 3 with the discrete representation as

$$T(z^{-1}) \times x(t) = R(z^{-1}) \times u(t) + M(z^{-1}) \times y(t) \tag{18}$$

where $x(t)$ and $y(t)$ are input and output variables. u is control output and $R(z^{-1})$, $T(z^{-1})$, $M(z^{-1})$ are polynomials to be determined and $R(z^{-1})$ is assumed to be a monic polynomial as

$$\begin{cases} R = 1 + rz^{-1} \\ M = m_0 + m_1 z^{-1} \end{cases} \tag{19}$$

The relationship between total force command input $f_{x(y)}$ and control output u for the motion system of X or Y table can thus be represented as

$$T(z^{-1}) \times f_{x(y)}(t) = R(z^{-1}) \times u(t) + M(z^{-1}) \times s_{x(y)}(t) \tag{20}$$

with the causal conditions to be met as deg $M \le R$ and deg $T \le R$ in the discrete time base. Suppose the desired closed loop pole and zero polynomials are A_m and B_m, respectively. The goal of the pole-placement design is to specify the desired closed loop poles so that system output perfectly tracks the input command to achieve high-precision position control performance. Therefore, the closed loop pole equation can be represented as

$$A(z^{-1})R(z^{-1}) + B(z^{-1})M(z^{-1}) = A_0(z^{-1})A_m(z^{-1}) \tag{21}$$

where $A_0(z^{-1})$ is referred as the observer polynomial that can be cancelled by zeros [14]. $A_m(z^{-1})$ is the desired pole polynomial. Causality conditions are denoted as follows,

$$\begin{cases} \deg A_0(z^{-1}) \times A_m(z^{-1}) \ge 2\deg A(z^{-1}) - 1 \\ \deg A_m(z^{-1}) - \deg B_m(z^{-1}) \ge \deg A(z^{-1}) - \deg B(z^{-1}) \end{cases} \tag{22}$$

where polynomial $B_m(z^{-1})$ contains the desired closed loop zeros.

Polynomials $A(z^{-1})$ and $B(z^{-1})$ contain system information for the denominator and numerator of the discrete transfer function described in Eq. (21), respectively, and the coefficients can be derived from online parameter estimation. $A(z^{-1})$ and $B(z^{-1})$ are coprime with $A(z^{-1})$ as a monic polynomial. The closed loop

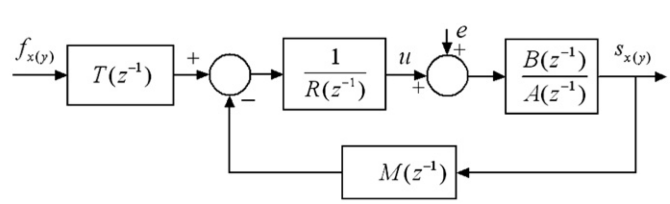

Fig. 3. Controller structure.

control output thus can be represented as [14],

$$s_{x(y)}(t) = \frac{B(z^{-1})T(z^{-1})}{A(z^{-1})R(z^{-1})+B(z^{-1})M(z^{-1})} \times f_{x(y)}(t) + \frac{B(z^{-1})M(z^{-1})}{A(z^{-1})R(z^{-1})+B(z^{-1})M(z^{-1})} \times e(t) \tag{23}$$

The main goal for the pole-placement design is to specify the desired closed-loop characteristic polynomial $A_0(z^{-1})A_m(z^{-1})$. A controller design with no cancellation of zeros is applied with the desired closed-loop transfer operator as

$$H_m(z^{-1}) = \beta \frac{b_0 + b_1 z^{-1}}{1 + a_{m1} z^{-1} + a_{m2} z^{-2}} \tag{24}$$

where $\beta=((1+a_{m1}+a_{m2})/(b_0+b_1))$ with β as the unit steady state gain. Then Eq. (24) becomes,

$$(1+a_1 z^{-1}+a_2 z^{-2})(1+r z^{-1})+(b_0+b_1 z^{-1})(s_0+s_1 z^{-1}) = (1+a_{m1} z^{-1}+a_{m2} z^{-2})(1+a_0 z^{-1}) \tag{25}$$

Solving for r, m_0 and m_1, we have [14],

$$r = \frac{a_0 a_{m2} b_0^2 + (a_2 - a_{m2} - a_0 a_{m1}) b_0 b_1}{b_1^2 - a_1 b_0 b_1 + a_2 b_0^2} + \frac{(a_0 + a_{m1} - a_1) b_1^2}{b_1^2 - a_1 b_0 b_1 + a_2 b_0^2} \tag{26}$$

$$m_0 = \frac{b_1(a_0 a_{m1} - a_2 - a_{m1} a_1 + a_1^2 + a_{m2} - a_1 a_0)}{b_1^2 - a_1 b_0 b_1 + a_2 b_0^2} + \frac{b_0(a_{m1} a_2 - a_1 a_2 - a_0 a_{m2} + a_0 a_2)}{b_1^2 - a_1 b_0 b_1 + a_2 b_0^2} \tag{27}$$

$$m_1 = \frac{b_1(a_1 a_2 - a_{m1} a_2 + a_{m2} a_0 - a_2 a_0)}{b_1^2 - a_1 b_0 b_1 + a_2 b_0^2} + \frac{b_0(a_{m2} a_2 - a_2^2 - a_0 a_{m2} a_1 + a_0 a_{m1} a_2)}{b_1^2 - a_1 b_0 b_1 + a_2 b_0^2} \tag{28}$$

Since the disturbances are relatively slow compared to the input command signal, polynomial $R(z^{-1})$ can be considered with factor of $(z^{-1}-1)$ as [14],

$$(z^{-1}-1)\nu(t) = \xi(t) \tag{29}$$

where $\xi(t)$ stands for the white noise. For cancellation of disturbances, the factor $(z^{-1}-1)$ can be included by requiring $R(z^{-1})$ with the form of,

$$R(z^{-1}) = (z^{-1}-1)R'(z^{-1}) \tag{30}$$

where $R'(z^{-1})$ is a polynomial. If the solutions are R^0, M^0 and T^0 and polynomials $R(z^{-1})$, $T(z^{-1})$ and $M(z^{-1})$ satisfy the following equations, then we have,

$$\begin{cases} R(z^{-1}) = (z^{-1}-1)R'(z^{-1}) = X(z^{-1})R^0(z^{-1}) + s(z^{-1})B(z^{-1}) \\ M(z^{-1}) = X(z^{-1})M^0(z^{-1}) - s(z^{-1})A(z^{-1}) \\ T(z^{-1}) = X(z^{-1})T^0(z^{-1}) \end{cases} \tag{31}$$

System output becomes,

$$s(t) = \frac{X(z^{-1})A_0(z^{-1})B_m(z^{-1})}{X(z^{-1})A_0(z^{-1})A_m(z^{-1})} \times F(t) + \frac{B_m(z^{-1})R'(z^{-1})}{X(z^{-1})A_0(z^{-1})A_m(z^{-1})} \times \xi(t) \tag{32}$$

It can be concluded from the above equation that the system output can track the input command in a desired manner and it is insensitive to the load disturbances with polynomial $X(z^{-1})$ and $A_0(z^{-1})$ if chosen as stable polynomials [15]. From the above deductions, the identification and control process can be depicted as shown in Fig. 4 for each axis of motion.

3.4. Convergence analysis of the adaptive controller

Convergence analysis for the identification process can be expressed as follows. For time invariant stochastic systems with

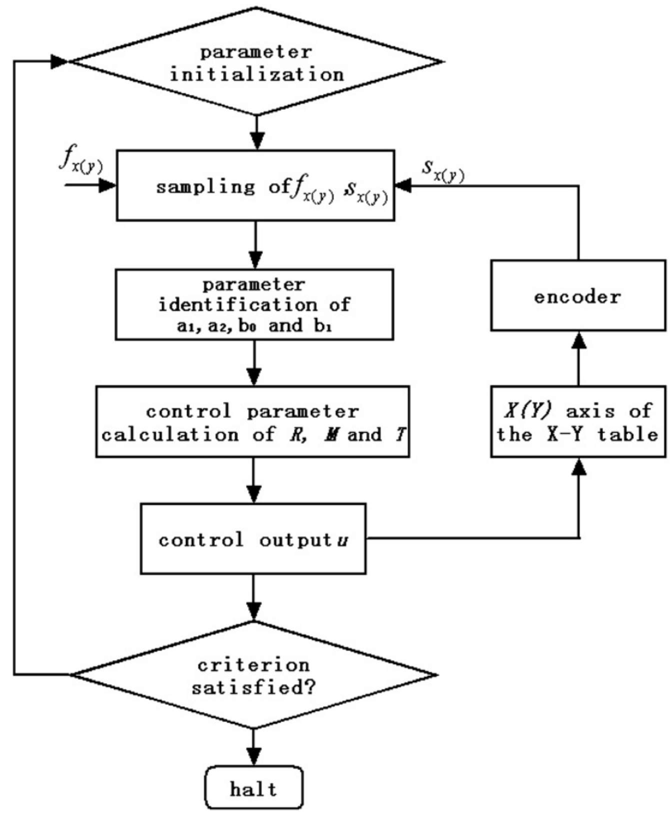

Fig. 4. Flow chart of identification and control.

the form of,

$$y(t) = \varphi^T(t) \times \theta(t-1) + \nu(t) \tag{33}$$

where $y(t)$ is the output of the system, θ is the time-varying parameter vector of the system to be identified with $\theta(t) \in R^n$, $\varphi(t) \in R^n$ is the regressive information vector and $\{\nu(t)\}$ is a stochastic noise sequence with zero mean. The least square algorithm with the forgetting factor for identifying the time-varying parameter vector of model (33) can be described as

$$\widehat{\theta}(t) = \widehat{\theta}(t-1) + P(t)\varphi(t)[y(t) - \varphi^T(t)\widehat{\theta}(t-1)] \tag{34}$$

$$P^{-1}(t) = \rho P^{-1}(t-1) + \varphi(t)\varphi^T(t), \quad 0 < \rho < 1 \tag{35}$$

where $\widehat{\theta}(t)$ denotes the estimate of $\theta(t)$, ρ is the forgetting factor, $P(t)$ is the covariance matrix with $P(0)=P_0>0$, and $\widehat{\theta}(0)$ is a random variable with $E[\widehat{\theta}^T(0)\widehat{\theta}(0)] \le M_0 < \infty$. $\{\nu(t)\}$ and $\widehat{\theta}(0)$ are independent.

Lemma 1. For the system and algorithm denoted in (33)–(35), respectively, if there exist constants $0 < \alpha \le \beta < \infty$ and an integer $N \ge n$ such that, for any $t > 0$, the following strong persistent excitation condition holds,

$$\alpha I \le \frac{1}{N} \sum_{i=1}^{N} \varphi(t+i)\varphi^T(t+i) \le \beta I \tag{36}$$

Then for $0 < \rho < 1$, $P(t)$ satisfies,

$$\frac{\rho^{N-1}}{1-\rho}\alpha I \le P^{-1}(t) \le \frac{N\beta}{1-\rho} I \tag{37}$$

Proof. From [16], we have,

$$P^{-1}(t) = \rho P^{-1}(t-1) + \varphi(t)\varphi^T(t) \le \sum_{i=1}^{t} \rho^{t-i}[N\beta I] + \rho^t P^{-1}(0)$$

$$= \frac{N\beta}{1-\rho} I + \rho^t \left[P_0{}^{-1} - \frac{N\beta}{1-\rho} I \right] \tag{38}$$

and,

$$NP^{-1}(t) = N \sum_{i=1}^{t} \rho^{t-i} \varphi(i)\varphi^T(i) + N\rho^t P^{-1}(0) \ge \sum_{i=1}^{t-N+1} \rho^{t-i}[N\alpha I] + N\rho^t P_0{}^{-1}$$
$$= \frac{\rho^{N-1}}{1-\rho} N\alpha I + N\rho^t \left[P_0{}^{-1} - \frac{\alpha}{1-\rho} I \right] \tag{39}$$

This completes the proof of Lemma 1.

Theorem 1. For the system denoted in (33) and the least square with forgetting factor (LSFF) algorithm depicted in (34) and (35), assume that condition (36) holds, then we can have,

$$\begin{cases} E[\nu^2(t)] = \sigma_\nu^2(t) \le \sigma_\nu^2 < \infty \\ E[\nu(t)\nu(i) = 0], \quad t \ne i \\ E[\varphi(t-i)\nu(t)] = 0, \quad i \ge 0 \end{cases} \tag{40}$$

The parameter change rate $w(t) \triangleq \theta(t) - \theta(t-1)$ is bounded, and $\{w(t)\}$ and $\{\nu(t)\}$ are independent, i.e.,

$$\begin{cases} E[\|w(t)\|^2] = \sigma_w^2(t) \le \sigma_w^2 < \infty \\ E[w(t)w^T(i)] = 0, \quad t \ne i, \quad E[w(t)\nu(i)] = 0 \end{cases} \tag{41}$$

Then as $t \to \infty$, the estimation error for $\widehat{\theta}(t)$ given by the LSFF is uniformly bounded as

$$E\left[\|\widehat{\theta}(t) - \theta(t)\|^2\right] \le 3\alpha^{-2}\rho^{2(t-N+1)}(1-\rho)^2 \|P_0{}^{-1}\|^2 M_0$$
$$+ \frac{3n(1-\rho)}{\alpha\rho^{N-1}} \sup_t E\left[\nu^2(t)\right] + \frac{3N^2\beta^2}{\alpha^2\rho^{2(N-1)}(1-\rho)^2} \sup_t E\left[\|w(t)\|^2\right] \triangleq f(\rho,t) \tag{42}$$

Detailed proof for condition (40) and (41) can be found in [17].

Theorem 2. For time invariant stochastic systems denoted in (33), assume that condition (36), (40) and (41) hold, then $[\hat{\theta}(t)]$ given by the LSFF algorithm satisfies [17],

$$E\left[\|\widehat{\theta}(t) - \theta\|^2\right] \le 2\alpha^{-2}\rho^{2(t-N+1)}(1-\rho)^2 \|P_0{}^{-1}\|^2 M_0$$
$$+ \frac{2n(1-\rho)}{\alpha\rho^{N-1}} \sigma_\nu^2 \triangleq f_2(\rho,t) \tag{43}$$

where σ_ν is the variance of $\nu(t)$. Eq. (43) denotes that for any $t > 0$, there exist constants $0 < \alpha \le \beta < \infty$, integer $N \ge n$ and a bounded constant M_0 that the LSFF algorithm gives a bounded mean square parameter estimation error (PEE) and the PEE converges to zero in a mean square sense [17].

Since the relationship of controller input and output can be expressed in Eq. (21), the adaptive controller output is obtained from adjusting $R(z^{-1})$, $T(z^{-1})$, and $M(z^{-1})$ based on the result of system identification results. If $A_m(z^{-1})$ that contains the desired closed loop poles are assigned with values enclosed by the unit circle in z-plane, the stability of the system based on the adaptive controller with the pole-placement algorithm can be ensured [14].

According to Eq. (7), the transfer function of the controlled plant can be further represented as

$$p(s) = \frac{K}{M_{x(y)}s^2 + B_{x(y)}s} \tag{44}$$

where K is a constant of 1000, the conversion of meter to millimeter.

The closed loop transfer function in continuous form then can be expressed as

$$G(s) = \frac{K}{M_{x(y)}s^2 + B_{x(y)}s + K} \tag{45}$$

With zero-order hold and the sampling time of T=0.001, the discrete transfer function can be obtained through z-transform as

$$G(z) = Z\left[\frac{1-e^{-Ts}}{s} \times G(s)\right] \tag{46}$$

4. Motion control system

4.1. Current controller

Considering the mechanical resonance of the mover from the machine, the bandwidth for the position controller is in the order of 10 Hz [18], therefore the two-time-scale control topology can be applied. Since the dynamics from the mechanical variable position is much slower than that of the electrical variable current, the electromagnetic variables can be considered to have remained in the steady states when all mechanical variables are taken into account. Therefore, the mechanical variables can be regarded as unchangeable when the electromagnetic variables are considered. The fast inner loop controller is employed to trace the currents through the motor windings with a sampling rate in the range of 10 kHz to correct current errors in time, while the slower outer loop position controller is used to track the reference position profiles.

For the current controller from either axis, three asymmetric bridge pulse width modulation (PWM) inverters are employed so that high dynamic response can be enjoyed independently in each phase for less current ripples [9]. At the side of PWM drive, the relationship between output current and input voltage for any one phase is,

$$\dot{i}_k = -\frac{R}{L_k(x,i)} \times i_k - \frac{\partial L_k(x,i)}{\partial x} \times \dot{x} \times \frac{1}{L_k(x,i)} \times i_k + \frac{1}{L_k(x,i)} \times V_k \tag{47}$$

where i_k is output current, V_k is input voltage. R is the winding resistance and L_k is phase inductance.

Eq. (47) can be further expressed as,

$$\dot{i}_k = -\frac{R}{L_k(x)} \times i_k + \frac{C}{L_k(x)} \times U_k \tag{48}$$

where C is the converter gain, and U_k is the controller input. The system plant can be represented as a first-order system,

$$H(s) = \frac{K_c}{L_k s + R} \tag{49}$$

where K_c is a constant. A modified proportional integral (PI) controller is applied for current regulation and the transfer function governing the controller is as follows,

$$G(s) = \frac{i_k(s)}{i_k^*(s)} = \frac{K_c(K_p s + K_i)}{L_k s^2 + (R + K_c K_p)s + K_c K_i} \tag{50}$$

Noticing that $K_c K_p \gg R$, the transfer function can be further simplified as

$$G(s) = \frac{i_k(s)}{i_k^*(s)} = \frac{K_c(K_p s + K_i)}{L_k s^2 + (R + K_c K_p)s + K_c K_i}$$
$$= \frac{(K_c K_p / L_k)s + (K_c K_i / L_k)}{s^2 + (K_c K_p / L_k)s + (K_c K_i / L_k)} \tag{51}$$

The coefficients K_p and K_i then can be determined from the damping factor and natural frequency of a typical second-order system as

$$K_p = \frac{2\varsigma\omega_n L_k}{K_c} \tag{52}$$

$$K_i = \frac{\omega_n^2 L_k}{K_c} \tag{53}$$

By choosing a proper value of K_p and K_i, the error will diminish to zero within a relatively short time and an overshoot free response can be achieved [8].

4.2. Speed controller design

In servo control applications, speed regulation is often employed to ensure that the machine follows a designated velocity reference profile and provides corresponding transients for the trajectory control loop. Between the inner current and outer trajectory loop, an intermediate loop of speed regulation is applied to regulate speed profiles and improve machine performance. For high-precision servo control applications of the proposed X–Y table, it is recommended that a proper speed control loop is implemented and inserted between the current and position control loop. To simplify the design of the speed control loop, it is assumed that the delay of the current loop is negligible due to the fact that usually the speed of response of the current loop is at least ten times faster than the response of the speed loop [8].

For any one axis of motion, neglecting load force, the transfer function that governs the speed behavior of the X–Y table can be represented as follows,

$$H(s) = \frac{K}{M_{x(y)} \times s + B_{x(y)}} \tag{54}$$

If a simple PI controller is applied for speed regulation of both axis of motion for transfer function $C(s)$, from the speed control block diagram depicted in Fig. 5, the transfer function of speed response can be represented as

$$\frac{V^*_{x(y)}}{V_{x(y)}} = K\frac{K_{vp} \times s + K_{vi}}{M_{x(y)} \times s^2 + (B_{x(y)} + K_{vp}) \times s + K_{vi}} \tag{55}$$

where K_{vp} and K_{vi} are the proportional and integral gain for the speed controller. The transfer function has two poles and only one zero. Since the integral gain K_{vi} is comparatively much smaller than the proportional gain K_{vp} [8], the only zero can be neglected and the transfer function can be further simplified as

$$\frac{V^*_{x(y)}}{V_{x(y)}} = K \cdot \frac{K_{vp} \cdot s}{M_{x(y)} \cdot s^2 + (B_{x(y)} + K_{vp}) \cdot s + K_{vi}} \tag{56}$$

The transfer function can be considered as a typical second-order control system with proportion K. The damping factor and natural frequency thus can be found as follows,

$$\begin{cases} 2\varsigma_s\omega_s = \frac{B_{x(y)} + K_{vp}}{M_{x(y)}} \\ \omega_s^2 = \frac{K_{vi}}{M_{x(y)}} \end{cases} \tag{57}$$

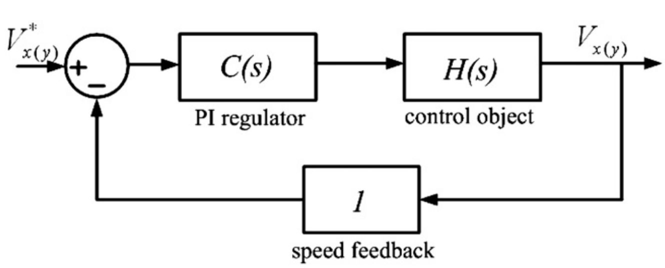

Fig. 5. Block diagram of speed control.

The coefficients from the speed control loop K_{vp} and K_{vi} then can be determined from Eq. (57). By choosing a proper value of K_{vp} and K_{vi}, the error will diminish to zero within a relatively short time and an overshoot-free response can be achieved [8]. With K_{vp} and K_{vi} gains are tuned as 5 and 0.2, respectively, an overshoot-free speed response for the X-table control system can be expected.

The experimental result for step response of the X-table can be found in Fig. 6. It takes the moving platform for 0.15 s to reach the destination velocity reference. The output waveform does not exhibit any overshoot with the proposed proportional and integral gains applied, which proves that the PI controller employed in the speed control loop maintains a desirable tracking response.

4.3. Position controller with multi-phase excitation and linearization

The operation of the outer position control loop is based on the assumption that the current and speed controllers have perfect tracking capability. For smooth operation with moderate force ripples and noise, a multi-phase excitation scheme is applied for each axis of motion and a linearization scheme is employed to calculate phase force command according to required total force command [18]. For each axis of motion, the multi-phase excitation scheme can be found in Table 2 [19].

Since SR motors behave highly nonlinear relationship of torque (force) respective to current and position, a linearization scheme is applied for each LSRM. To optimize between computation efficiency and memory consumption, a pair of low-resolution 2D 27×27-matrix look-up tables are used for each axis of motion with bi-linear interpolation to calculate the intermediate values. This produces a considerably low worst-case deviation from the original nonlinear function and the output values can also follow a smooth profile [18]. The overall position control diagram with the proposed adaptive controller can thus be derived as shown in Fig. 7. The multi-phase excitation scheme first determines which phase(s) should be excited according to current position $s_{x(y)}$ and force command $f_{x(y)}$. Then force reference values $f_k(k{=}a,b,c)$ for the excited phase(s) is assigned according to Table 2 from the force command for the X or Y table. Next, the inverse relationship of current command $i_k^*(k=a,b,c)$ from each phase can be derived from the 2D look-up table. Last, actual current $i_k(k{=}a,b,c)$ are output from the current controllers.

5. Implementation results

The experiment is implemented with a PCI-based dSPACE DS1104 controller card. The interface circuit from the control board consists of two 24-bit digital incremental encoder channels to provide velocity and position feedback from each axis. The current drivers receive command signal from the digital-to-analog converters and supply current excitations to each phase for two-axis of motion.

The control algorithm is programmed in *MATLAB/SIMULINK* platform and can be converted into *C* code after compilation and downloaded to the DSP chip of the controller card. Control parameters are regulated online and current status of the control system are displayed accordingly.

5.1. Parameter identification

Since the LSRM from each axis of motion cannot self start under the adaptive algorithm, PID regulator is implemented for closed loop position control and online parameter identification. The position algorithm is switched to the adaptive controller after parameter identification is complete. As shown in Fig. 8 the

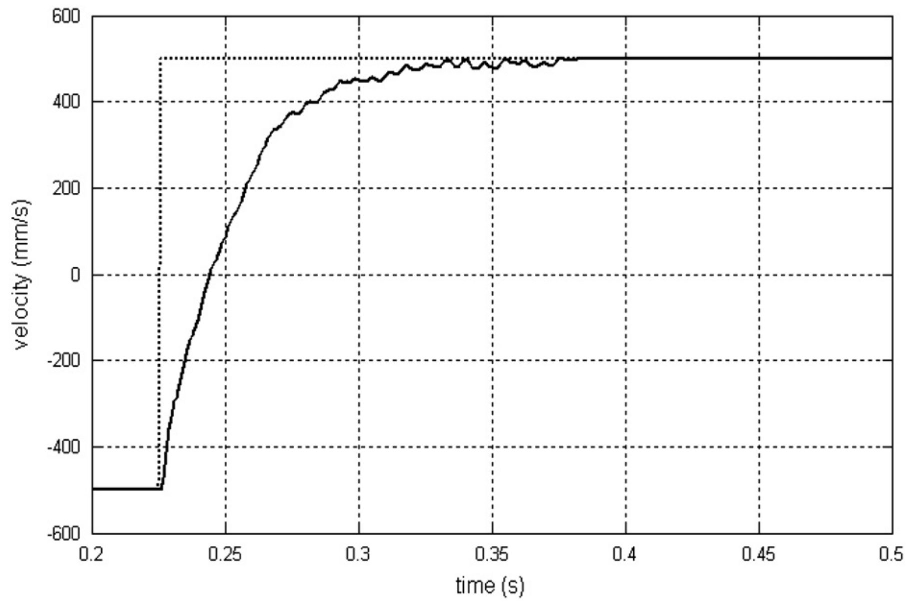

Fig. 6. Experimental results of speed response.

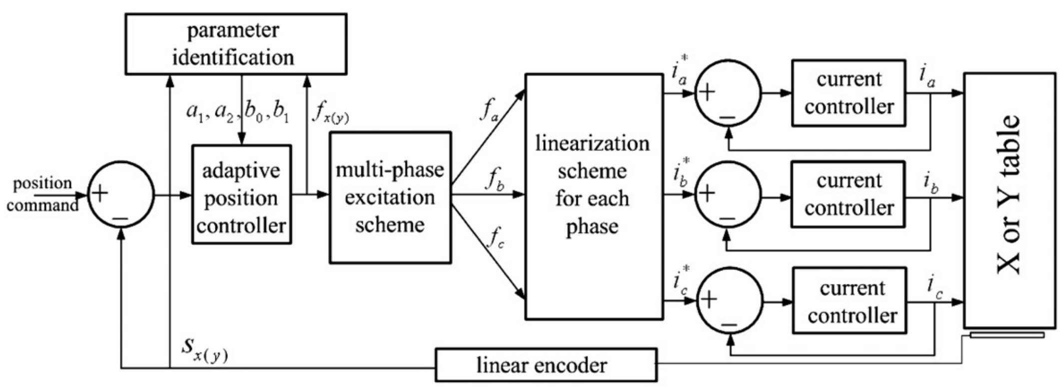

Fig. 7. Position control block diagram for one axis of the machine.

Table 2
Multi-phase excitation scheme for *X* or *Y* table.

Range (mm)	Force command ($f>0$)	Force command ($f<0$)
$0<x(y)\le 2$	$f_b=f$	$f_a=f\times(\sqrt{\sin\alpha}/\sqrt{\sin\alpha}+\sqrt{\sin\gamma})$ $f_c=f\times\sqrt{\sin\gamma}/\sqrt{\sin\alpha}+\sqrt{\sin\gamma}$
$2<x(y)\le 4$	$f_b=f\times(\sqrt{\sin\beta}/\sqrt{\sin\beta}+\sqrt{\sin\gamma})$ $f_c=f\times(\sqrt{\sin\gamma}/\sqrt{\sin\beta}+\sqrt{\sin\gamma})$	$f_a=f$
$4<x(y)\le 6$	$f_c=f$	$f_a=f\times(\sqrt{\sin\alpha}/\sqrt{\sin\alpha}+\sqrt{\sin\beta})$ $f_b=f\times(\sqrt{\sin\beta}/\sqrt{\sin\alpha}+\sqrt{\sin\beta})$
$6<x(y)\le 8$	$f_a=f\times(\sqrt{\sin\alpha}/\sqrt{\sin\alpha}+\sqrt{\sin\gamma})$ $f_c=f\times(\sqrt{\sin\gamma}/\sqrt{\sin\alpha}+\sqrt{\sin\gamma})$	$f_b=f$
$8<x(y)\le 10$	$f_a=f$	$f_a=f\times(\sqrt{\sin\beta}/\sqrt{\sin\beta}+\sqrt{\sin\gamma})$ $f_c=f\times(\sqrt{\sin\gamma}/\sqrt{\sin\gamma}+\sqrt{\sin\beta})$
$10<x(y)\le 12$	$f_a=f\times(\sqrt{\sin\alpha}/\sqrt{\sin\alpha}+\sqrt{\sin\beta})$ $f_b=f\times(\sqrt{\sin\beta}/\sqrt{\sin\alpha}+\sqrt{\sin\beta})$	$f_c=f$

Note: $\alpha=2\pi\times x(y)/12$, $\beta=\alpha-2\pi/3$, $\gamma=\alpha-4\pi/3$, 0 mm is the fully aligned position from phase a.

identification results under PID regulator, it takes about 1.5–2 s for all parameters to converge. Since mechanical and electrical parameters are distinct from each axis of motion, the corresponding identification results are different. After the identification process is stable, the adaptive controller can be implemented to replace the PID method.

5.2. Performance test

For comparison of control performance between PID and the adaptive control method, control variables from both PID and adaptive control are regulated for the same state and they remain unchanged though operation conditions are varied. Parameters

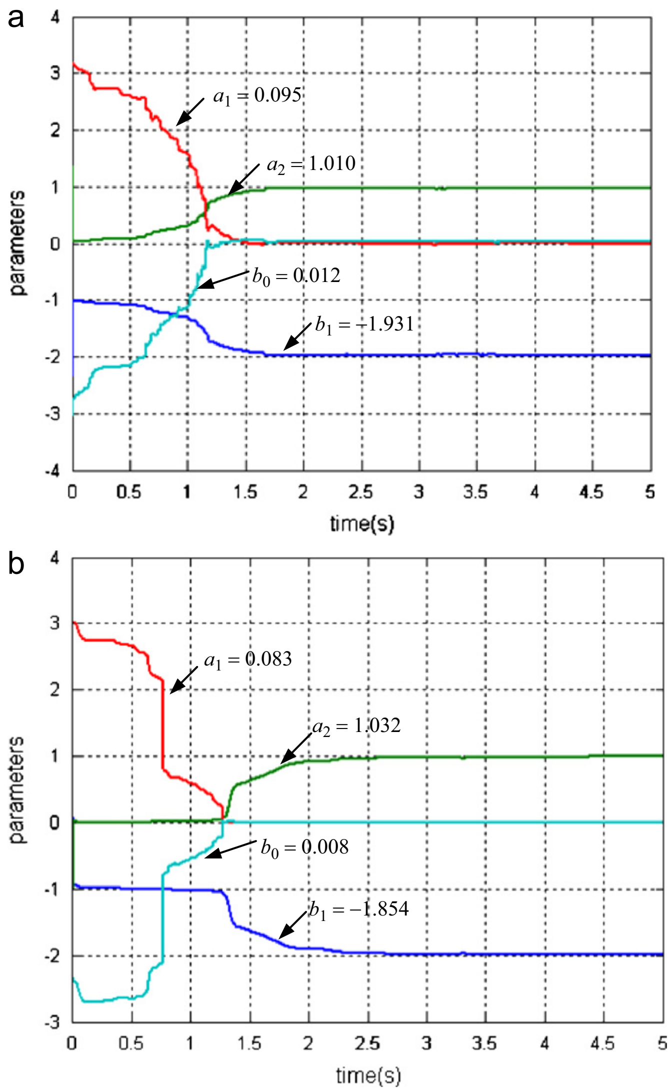

Fig. 8. Results of parameter identification (a) *X* table (b) *Y* table.

Table 3
Parameter regulation.

Parameter	Nominal state (20 mm, 3 s)	
	X	*Y*
P	0.2	0.9
D	1.1	9.0
I	0.001	0.002
a_{m1}	−1.93	−1.935
a_{m2}	0.938	0.938
b_{m0}	−0.850	−0.850
b_{m1}	−0.800	−0.800
ρ	0.99	0.99

for square wave operation with amplitude of 20 mm and period of 3 s are regulated as the nominal state with parameters tabulated in Table 3 and dynamic error profiles shown in Fig. 7 for each axis of motion. It is clear from the shifted response waveforms from the two controllers that overshoots are relatively huge with large static errors for the PID controller for each axis of motion. However, the performance under the adaptive controller provides a smooth dynamic transition and a static error of ± 2 and ± 2.5 μm for *X* and *Y* axis, respectively. The parameters for PID and adaptive controller are illustrated in Table 3 and all remain unchanged for composite command references. The dynamic response for each axis of motion can be found in Fig. 9.

For actual operations under composite command of the machine, command for each axis can be designed independently from a decoupled motion structure. The response of the *X*–*Y* machine when drawing a line is shown in Fig. 10 under the position command of square waveform with 0°phase difference. Since there are sharp transitions for a square profile, dynamic performance deteriorates at each corner from the PID controller. However, the response from the adaptive controller provides a reasonable overshoot and dynamic errors.

Sinusoidal command reference is also selected for performance test. Under the compound command signal, the table will draw a circle with uniform position command and a line with 180° phase difference as shown in Fig. 11. It is clear that the

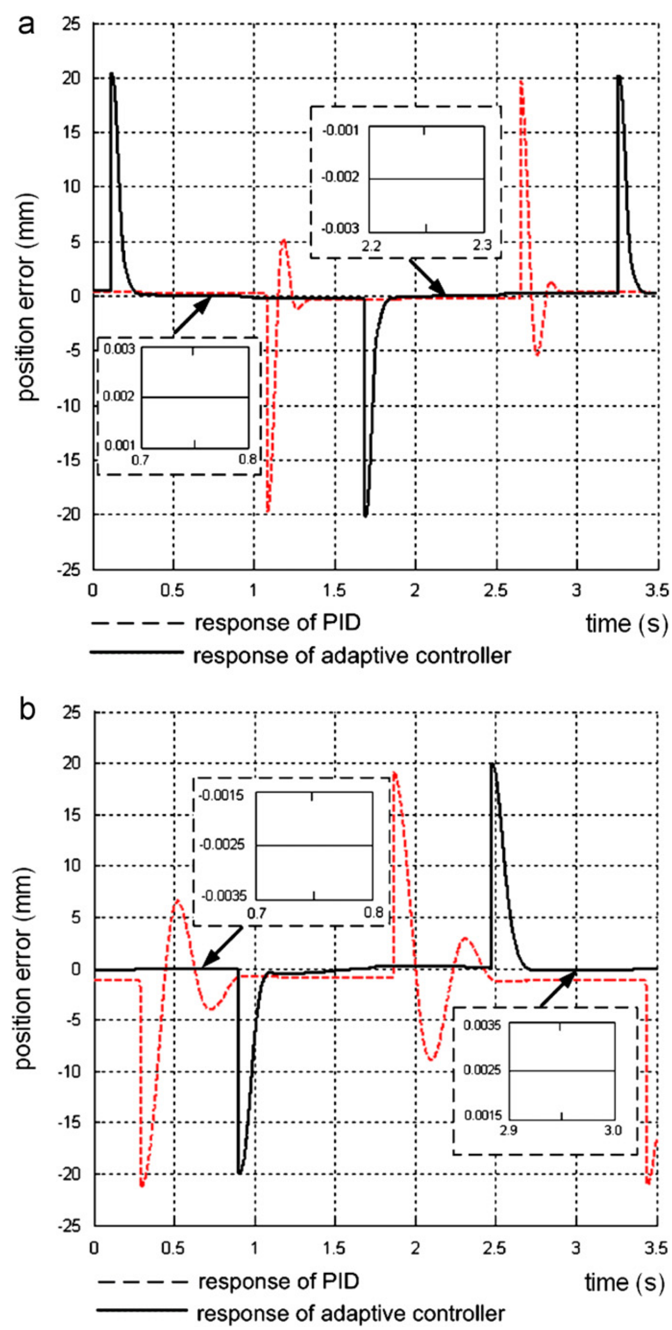

Fig. 9. Dynamic response from each axis of motion (a) *X* axis and (b) *Y* axis.

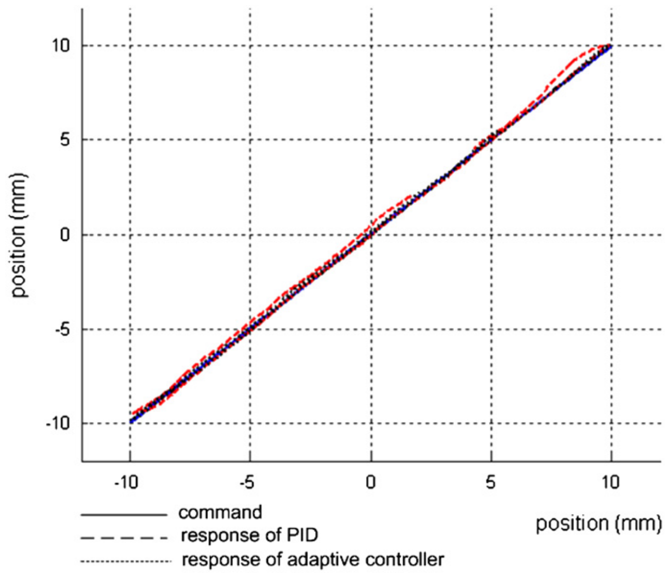

Fig. 10. Response of the machine—line.

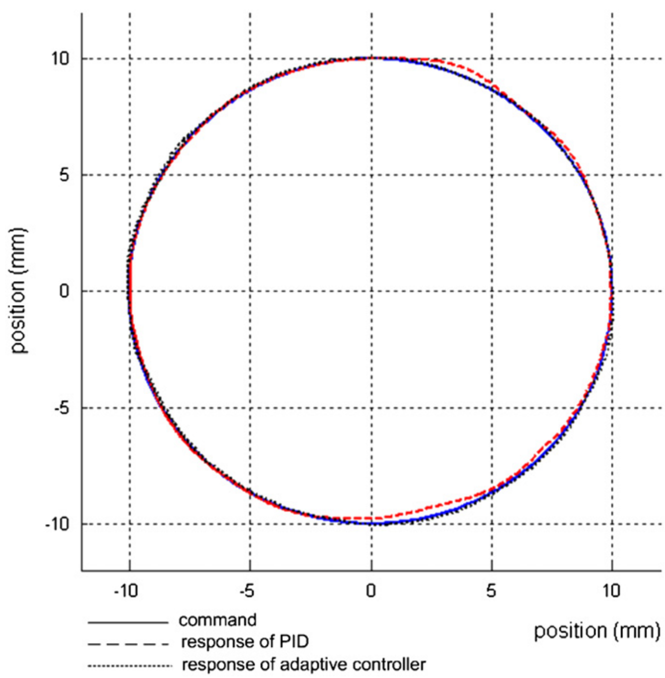

Fig. 11. Trajectory response—circle.

tracking profiles are more precise under the adaptive controller than PID.

5.3. Test of robustness

To further test machine performance under the interference environment, a constant force disturbance of 15 N is added before the position controller block to the *X* axis table with all control parameters unchanged. To avoid severe change of operation under disturbances, a third-order *S*-profile with smooth transitions from rising and declining part of the waveform is applied as the position command [20]. As shown in Fig. 12, the tracking profile under PID controller continuously experience relatively large errors and it is not capable of correction for such disparities. However, the adaptive controller is able to compensate force

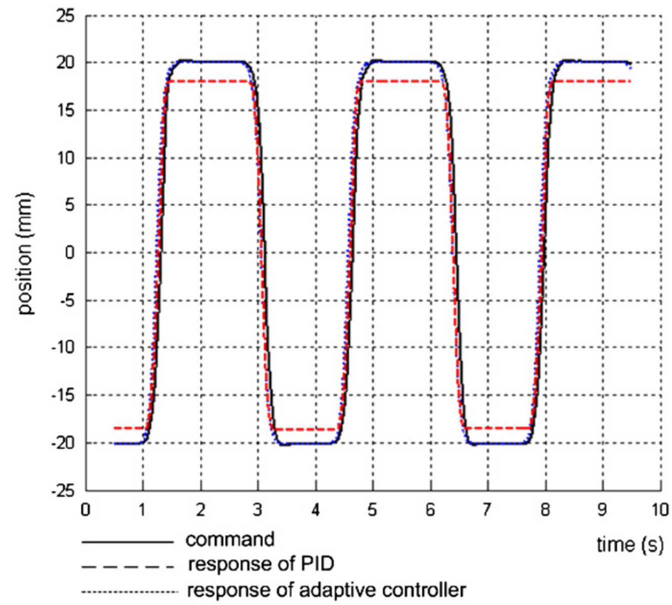

Fig. 12. Trajectory response under disturbance.

disturbance with a reasonable dynamic and static response at the same time.

6. Conclusion

The design methodology for LSRM-based *X–Y* machine has been discussed in this paper. Since traditional machines with rotary motors and mechanical translators have the disadvantages of high cost, complex structure and require frequent adjustment and maintenance, it is expected that the LSRM-based *X–Y* machine will be an ideal alternative to the traditional methods for 2D high-precision translational applications. With the development of the adaptive controller, high-precision position control can be achieved. It can be expected the cost of the processing components and parts will be significantly reduced if the proposed *X–Y* table can be successfully employed in the advanced manufacture area.

Acknowledgements

The authors would like to thank the National Natural Science Foundation of China and Guangdong Natural Science Foundation for the sponsoring of this research project under the project code 51007059 and S2011010001208; the authors would also like to thank Hong Kong Research Grants Council and Shenzhen government fund PolyU 5140/07E, JC201005280390A and ZYB200907080073A for support.

References

[1] Otten G, Vries JA, Amerongen JV, Rankers AM, Gaal EW. Linear motor motion control using a learning feedforward controller. IEEE/ASME Transactions on Mechatronics 1997:179–87.
[2] Wang Limei, Wu Zhitao, Liu Chunfang. Trajectory tracking for direct drive *X–Y* table using T-S recurrent fuzzy network controller. International conference on mechatronics and automation, ICMA 2009, pp. 3000–4.
[3] Hanafi D, Tordon M, Katupitiya J. An active axis control system for a conventional CNC machine. IEEE/ASME International Conference in Advanced Intelligent Mechatronics 2003:1188–93.
[4] Chancharoensook P, Rahman MF. A high-precision speed control of a four-phase switched reluctance motor drive using closed-loop controllers of

instantaneous torque and current. 30th Annual Conference of IEEE Industrial Electronics Society, IECON 2004, pp. 2355–60.
[5] Divandari M, Koochaki A, Maghsoodloo A, et al. High performance SRM drive with hybrid observer and fuzzy logic torque ripple minimization. IEEE International Symposium on Industrial Electronics 2007:1230–5 ISIE.
[6] Hwu KI, Liaw CM. Robust quantitative speed control of a switched reluctance motor drive. IEE Proceedings on Electric Power Applications 2001;148(4): 345–53.
[7] Zhao SW, Cheung NC, Gan WC, Yang JM. High precision position control of a linear switched reluctance motor using a self-tuning regulator. IEEE Transactions on Power Electronics 2010;25(11):2820–7.
[8] Krishnan R. Switched reluctance motor drives: modeling, simulation, analysis, design, and applications. Boca Raton, FL: CRC Press; 2001 pp. 15–21.
[9] Boldea I, Nasar SA. Linear electric actuators and generators. Cambridge, UK: Cambridge Univ. Press; 1997 pp. 105–15.
[10] Liu Cheng-Tsung, Kuo Jian-Long. Experimental investigation and 3-D modelling of linear variable-reluctance machine with magnetic-flux decoupled windings. IEEE Transactions on Magnetics 1994;30(6):4737–9 Part 1–2.
[11] Ding Zhigang. Linear stepping motors—principle, control and applications. Beijing: Mechanical Industry publisher; 2001 pp. 87–8.
[12] Sun ZG, Cheung NC, Zhao SW, Gan WC. Magnetic analysis of switched reluctance actuators in levitated linear transporters. IEEE Transactions on Vehicular Technology 2010;59(9):4280–8.
[13] Ljung Lennart. System identification—theory for the user. 2nd ed.Prentice-Hall; 1999 pp. 45–7.
[14] Åström KJ, Wittenmark B. Adaptive control. Addison-Wesley; 1995, pp. 120–5.
[15] Wilson SS, Carnal CL. System identification with disturbances. Proceedings of the 26th southeastern symposium—system theory, 1994, pp. 502–6.
[16] Ding F, Yang JB. Comments on martingale hyper-convergence theorem and the convergence of forgetting factor least square algorithm. Control Theory and Applications 1999;16(4):569–72 in Chinese.
[17] Ding Feng, Ding Tao. Convergence of forgetting factor least square algorithms. IEEE Pacific Rim Conference on Communications, Computers and Signal Processing 2001;2:433–6.
[18] Pan JF, Cheung NC, Yang Jinming. High-precision position control of a novel planar switched reluctance motor. IEEE Transactions on Industrial Electronics 2005;52(6):1644–52.
[19] Husain I, Ehsani M. Torque ripple minimization in switched reluctance motor drives by PWM current control. IEEE Transactions on Power Electronics 1996;11(1):83–8.
[20] Gan Wai-Chuen, Cheung Norbert C, Qiu Li. Position control of linear switched reluctance motors for high-precision applications. IEEE Transactions on Industry Applications 2003;39(5):1350–62.